Imaging the fault zones of the 2000 western Tottori earthquake by a new inversion method to estimate three-dimensional distribution of the scattering coefficient

doi: 10.1029/2003JB002761

Imaging the fault zones of the 2000 western Tottori earthquake by a new inversion method to estimate three-dimensional distribution of the scattering coefficient

Youichi Asano[1] and Akira Hasegawa

Research Center for Prediction of Earthquakes and Volcanic Eruptions, Graduate School of Science, Tohoku University, Sendai, Japan

Received 25 August 2003; revised 31 December 2003; accepted 21 April 2004; published 24 June 2004.

[1] We developed an inversion method to estimate the spatial variation of scattering coefficient from observed envelopes of *S* coda waves. Synthetic envelopes are calculated on the basis of the single scattering theory, assuming double-couple sources and a one-dimensional depth-dependent velocity structure. In our algorithm, we evaluated scattering attenuation taking spatial variation of scattering coefficient into consideration in order to model energy attenuation by passing through the localized anomalous zones with high scattering coefficients. The inversion method was applied to the seismograms in and around the focal area of the 2000 western Tottori earthquake with *M* 7.3. Obtained results show that there exist several zones with large scattering coefficient zones (LSZs). One of the most predominant LSZ is located along and around the fault zone of the *M* 7.3 earthquake in the upper crust. This LSZ suggests the existence of damaged zones in the main shock fault. Within this LSZ, an exceptionally small scattering coefficient area was detected. This area corresponds to an asperity with a large amount of coseismic slip of the main shock. Other prominent LSZs are detected in the mid to lower crust below the northwestern part of the main shock fault. In addition, LSZs are distributed in a seismic low-velocity zone, near Quaternary volcanoes, and near hypocenters of deep low-frequency microearthquakes. Some of the imaged LSZs are probably related to local concentration of fluid in the crust. *INDEX TERMS:* 7260 Seismology: Theory and modeling; 7205 Seismology: Continental crust (1242); 7209 Seismology: Earthquake dynamics and mechanics; 8180 Tectonophysics: Tomography; *KEYWORDS:* fault zone, crustal heterogeneity, coda envelope

Citation: Asano, Y., and A. Hasegawa (2004), Imaging the fault zones of the 2000 western Tottori earthquake by a new inversion method to estimate three-dimensional distribution of the scattering coefficient, *J. Geophys. Res.*, *109*, B06306, doi:10.1029/2003JB002761.

1. Introduction

[2] Seismic coda, which is observed following the arrivals of direct *P* and *S* waves, is considered to be a superposition of incoherent scattered waves caused by inhomogeneous structures of the Earth [*Aki*, 1969; *Aki and Chouet*, 1975]. The radiative transfer theory is one possible approach to evaluate the energy density of the coda in time and space domains. Approximating random phases for the scattered waves, the theory evaluates the transport energy of the waves through a medium. *Sato* [1977] proposed a formulation to evaluate coda energy density on the basis of a single scattering model, which is a special case of the radiative transfer theory. He applied the formulation to the case of separated locations of source and receiver, and showed that synthetic seismogram envelopes calculated by his model explain observed seismogram envelopes of *S* coda. An integral equation of the radiative transfer theory, including multiple scattering processes for the case of an impulsive energy radiation at a source was presented by *Zeng et al.* [1991]. It is known that the analytical solution of energy density can be derived from the integral equation in a uniformly random media with a constant seismic velocity [e.g., *Sato and Fehler*, 1998]. These previous studies have dealt with scattered energy in uniformly random media, while there are also studies which addressed with scattering problem in nonuniformly random media. Coda modeling using Monte Carlo simulation for the multiple scattering process is one of such examples [*Abubakirov and Gusev*, 1990; *Hoshiba*, 1991]. Inhomogeneous structures with nonuniform randomness were also suggested in order to explain the features of the observed *S* coda [e.g., *Nishigami*, 1991, 1997, 2000; *Obara*, 1997; *Chen and Long*, 2000].

[3] *Obara* [1997] developed a method for estimating energy density of *S* coda in nonuniformly random media. In the method, the energy density is expressed as a summation of scattered energy contributions from many

[1]Now at the National Research Institute for Earth Science and Disaster Prevention, Tsukuba, Japan.

0148-0227/04/2003JB002761$09.00

small cubic blocks, which compose the crust and upper mantle of the target area. He presented a model which explains observed *S* coda envelopes including reflected waves from the upper boundary of the Pacific plate.

[4] *Nishigami* [1991] dealt with the energy perturbation in the general decay of the *S* coda. He developed an inversion method to estimate spatial perturbation of scattering coefficient from the energy perturbation. *Nishigami* [2000] applied this method to the observed envelopes, in the local seismic network around the San Andreas fault system, and discussed a relationship between the spatial variation of the scattering coefficient and the locations of fault segments. These studies have shown the effectiveness of the coda envelope data in estimating inhomogeneous structures of the Earth. Although the method presented by *Nishigami* [1991] has an advantage that we can ignore the effects of both scattering attenuation and intrinsic absorption due to the procedure of removing general coda decay, the energy perturbation of the *S* coda after the procedure will cause the loss of information about absolute values and spatially gentle variations of the scattering coefficient. Another problem of the method is that the general coda decay should be calculated analytically. In the calculation of such decay, *Nishigami* [1991] assumed isotropic source radiation in a constant velocity structure according to *Sato* [1977]; however we prefer to use a depth-dependent velocity structure and double-couple source models for imaging localized scatterers with high resolution. Such complicate models cannot be used in the method by *Nishigami* [1991] because of the problem on the analytical calculation of coda decay. In order to prevent the problem, we developed a new inversion method without the procedure of removing general coda decay. In our method, we can easily take into consideration depth-dependent velocity structures, double-couple sources, and scattering attenuation caused by three-dimensional (3-D) distribution of scattering coefficients. Absolute values of the scattering coefficient can be also obtained, although intrinsic absorption parameter has to be assumed. The absolute values may provide important information to compare and discuss the extent of the heterogeneity among different studies in various tectonic fields.

2. Methods

2.1. Synthetic and Observed Energy Density

[5] In this section, we explain a method for synthetic seismogram envelopes. We divided a three-dimensional target region into many cubic blocks, each having their respective scattering coefficient. Coda energy density can be estimated from the summation of contributions of each block according to *Obara* [1997], and the contributions are evaluated on the basis of the single scattering model [e.g., *Sato*, 1977]. Coda energy density $E_{mn}^{\mathrm{syn}}(t_i)$ from the *m*th hypocenter, at the *n*th station, and in the *i*th lapse time window with a starting time t_i and a length of t^{win} is expressed as

$$E_{mn}^{\mathrm{syn}}(t_i) = \sum_{j=1}^{N_{\mathrm{block}}} W_m^{\mathrm{hyp}} R_{mj}^{\mathrm{hyp}} R_{mnj}^{\mathrm{sca}} B_{mnj}(t_i) \cdot G_{mnj} A_{mnj} \Delta V_j^{\mathrm{block}} g_j^{\mathrm{block}} / V_s^{\mathrm{stn}} t^{\mathrm{win}}, \quad (1)$$

where $\Delta V_j^{\mathrm{block}}$ and g_j^{block} are the volume and scattering coefficient of the *j*th block. W_m^{hyp}, R_{mj}^{hyp}, and R_{mnj}^{sca} are the source radiation energy, the effect of source radiation pattern, and the effect of angular dependency of scattering coefficient, respectively (see also Figures 1a and 1b). Although nonisotropic scattering model can be easily introduced in the calculation of the energy density, we adopted isotropic scattering model and set R_{mnj}^{sca} to be 1 as follows. The summation is accomplished over N_{block} small blocks set in the subsurface, and reflections on the free surface are neglected.

[6] $B_{mnj}(t_i)$ means a contribution index and is defined as

$$B_{mnj}(t_i) = \int_{t_i}^{t_i + t^{\mathrm{win}}} \delta\left(t - t_{mnj}^{\mathrm{scattered}}\right) dt, \quad (2)$$

where $t_{mnj}^{\mathrm{scattered}}$ is the travel time of the scattered wave propagating along the ray path from the *m*th hypocenter to the *n*th station through the center of the *j*th block. If there is an arrival of the scattered energy in the *i*th lapse time window, $B_{mnj}(t_i)$ is 1, while it is 0 otherwise. G_{mnj} is the geometrical spreading factor along the path; $t_{mnj}^{\mathrm{scattered}}$ and G_{mnj} were calculated analytically, assuming a 1-D velocity structure with linear function of depth. It is important to calculate $t_{mnj}^{\mathrm{scattered}}$ and G_{mnj} analytically in order to decrease the amount of calculation in our algorithm, because for each hypocenter-station pair N_{block} calculations of these two values are required. V_s^{stn} in equation (1) is the *S* wave velocity at 0-km depth.

[7] A_{mnj} represents the attenuation effect along the same ray as the case of $t_{mnj}^{\mathrm{scattered}}$. We divided the ray into N_{seg} small segments to express the total attenuation effect along the path as the product of the effects in each segment with the length of $\Delta l_k^{\mathrm{seg}}$. The total attenuation effect along the path can be described as

$$A_{mnj} = \prod_{k=1}^{N_{\mathrm{seg}}} \exp\left[-\left(Q_{\mathrm{int}}(\omega)^{-1}\omega / V_{Smnjk}^{\mathrm{seg}} + g_{mnjk}^{\mathrm{seg}}\right)\Delta l_k^{\mathrm{seg}}\right], \quad (3)$$

where $V_S^{\mathrm{seg}}{}_{mnjk}$ and g_{mnjk}^{seg} are *S* wave velocity and total scattering coefficient in the *k*th segment along the path. $Q_{\mathrm{int}}(\omega)^{-1}$ and ω are the spatially uniform intrinsic absorption parameter and the characteristic angular frequency (constant) of monochromatic scattered waves. The primary and secondary terms in the parenthesis of equation (3) mean contributions of intrinsic absorption and scattering attenuation, respectively. It is difficult to independently estimate the intrinsic absorption parameter and the scattering coefficient in the following inversion. Therefore the intrinsic absorption parameter is not estimated but assumed to be a priori value, which may be selected with respect to the previous results [e.g., *Fehler et al.*, 1992; *Mayeda et al.*, 1992; *Hoshiba*, 1993].

[8] Equations (1) and (3) include the scattering coefficients g_j^{block} in the *j*th block and g_{mnjk}^{seg} in the segment, respectively. Although g_j^{block} and g_{mnjk}^{seg} are different variables, we prefer to have only one variable related to scattering coefficient. Therefore we define a new variable g_l^{grid} of scattering coefficient in the *l*th grid set in the same target region. The grids are structured with a larger grid separation than the block size and the length segment as

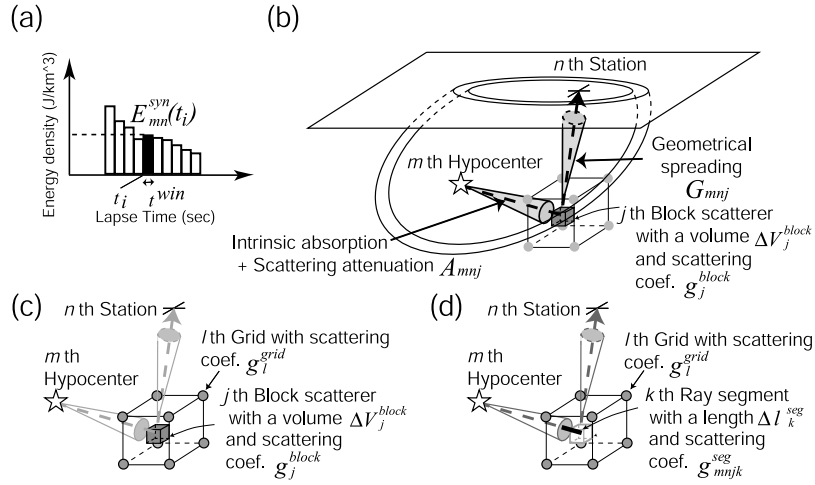

Figure 1. Schematic illustration of (a) synthetic energy density, (b) single scattering on a block scatter, and linear interpolation of scattering coefficients in (c) a block and (d) a segment using scattering coefficients in adjacent eight grids.

shown in Figures 1c and 1d. The scattering coefficients g^{block}_j and g^{seg}_{mnjk} are expressed by equations (4) and (5), respectively, which mean linear interpolation using values of g^{grid}_l in adjacent eight grids:

$$g^{\text{block}}_j = \sum_{l=1}^{N_{\text{grid}}} T^{\text{block}}_{lj} g^{\text{grid}}_l \tag{4}$$

$$g^{\text{seg}}_{mnjk} = \sum_{l=1}^{N_{\text{grid}}} T^{\text{seg}}_{mnjkl} g^{\text{grid}}_l, \tag{5}$$

where N_{grid} is the number of grids. T^{block}_{lj} and T^{seg}_{mnjkl} are weighting matrices for the interpolation, respectively. By substituting equation (4) into equation (1) and assuming isotropic scattering model ($R^{\text{sca}}_{mnj} = 1$), the synthetic energy density is expressed as a function of g^{grid}_l:

$$E^{\text{syn}}_{mn}(t_i) = \sum_{j=1}^{N_{\text{block}}} W^{\text{hyp}}_m R^{\text{hyp}}_{mj} B_{mnj}(t_i) G_{mnj} A_{mnj} \Delta V^{\text{block}}_j \cdot \left(\sum_{l=1}^{N_{\text{grid}}} T^{\text{block}}_{lj} g^{\text{grid}}_l \right) / V^{\text{stn}}_s t^{\text{win}}. \tag{6}$$

We evaluated the observed energy density using three-component seismograms observed at each station. The observed energy density E^{obs}_{mnj} from the mth hypocenter, at the nth station, and in the ith lapse time window expressed as

$$E^{\text{obs}}_{mn}(t_i) = \rho^{\text{stn}}_n S^{\text{stn}^2}_n \sum_{p=1}^{N_{\text{win}}} \sum_{q=1}^{3} \nu(t_i + p\delta t^{\text{samp}})^2_{mnq} / N_{\text{win}}, \tag{7}$$

where $v(t)_{mnq}$ is a time series of velocity amplitude (seismograph) for the mth hypocenter, the nth station, and the qth component; p means the sample number in a lapse time window for the evaluation of averaged coda energy density; ρ^{stn}_n, $S^{\text{stn}^2}_n$, δt^{samp}, and N_{win} are medium density at 0-km depth, site factor, sampling interval in seconds, and length of the lapse time window in samples, respectively. The time length of the lapse time window t^{win} in equation (1) is expressed as

$$t^{\text{win}} = N_{\text{win}} \delta t^{\text{samp}}. \tag{8}$$

2.2. Observation Equation

[9] In this section, we derive an equation which connects synthetic and observed energy densities. An equation for data may be derived from equations (6) and (7), but it is difficult to simultaneously estimate the source radiation energy W^{hyp}_m, the medium density ρ^{stn}_n, and the site factor $S^{\text{stn}^2}_n$. Therefore we obtain the following observation equation employing the conventional coda normalization method [*Aki*, 1980]:

$$\frac{E^{\text{syn}}_{mn}(t_i)}{\frac{1}{N_{\text{later}}} \sum_{k}^{\text{later}} E^{\text{syn}}_{mn}(t_k)} \approx \frac{E^{\text{obs}}_{mn}(t_i)}{\frac{1}{N_{\text{later}}} \sum_{k}^{\text{later}} E^{\text{obs}}_{mn}(t_k)}, \tag{9}$$

where the denominators of both sides of equation (9) show the synthetic and the observed energy densities of a later part of the S coda, respectively. Applying equation (9), we assume that the energy density of the later part of the S coda is approximately independent of source and station locations. When the spatial extent of the scattering shells evaluated for the later coda is grossly sufficiently larger than that of the distribution of sources and stations, the shells sample the nearly equivalent volume in the crust and the upper mantle. In this case, the energy density of the later coda is insensitive to the spatially nonuniform randomness of inhomogeneous structures, justifying the above assumption. An operator $1/N_{\text{later}} \sum_k^{\text{later}}$ means averaging over several lapse time windows corresponding to later portions of the S coda. By substituting equations (6)

and (7) into equation (9), W_m^{hyp}, ρ_n^{stn}, and $S_n^{\mathrm{stn}^2}$ are cancelled. Thereby equation (9) becomes

$$\frac{\sum_{j=1}^{N_{\mathrm{block}}}\left[R_{mj}^{\mathrm{hyp}}B_{mnj}(t_i)G_{mnj}A_{mnj}\left(\sum_{l=1}^{N_{\mathrm{grid}}}T_{jl}^{\mathrm{block}}g_l^{\mathrm{grid}}\right)\right]}{\sum_{k}^{\mathrm{later}}\sum_{j=1}^{N_{\mathrm{block}}}\left[R_{mj}^{\mathrm{hyp}}B_{mnj}(t_k)G_{mnj}A_{mnj}\left(\sum_{l=1}^{N_{\mathrm{grid}}}T_{jl}^{\mathrm{block}}g_l^{\mathrm{grid}}\right)\right]} \approx \frac{\sum_{p=1}^{N_{\mathrm{win}}}\sum_{q=1}^{3}\nu(t_i+p\delta t^{\mathrm{samp}})_{mnq}^2}{\sum_{k}^{\mathrm{later}}\sum_{p=1}^{N_{\mathrm{win}}}\sum_{q=1}^{3}\nu(t_k+p\delta t^{\mathrm{samp}})_{mnq}^2}. \quad (10)$$

Since our observation is $v(t)$ in the right-hand side of equation (10), we may write it symbolically by

$$F\left(g_l^{\mathrm{grid}}\right)_{mni} \approx d_{mni}. \quad (11)$$

The final formulation, equation (10) or (11), is a nonlinear equation of g_l^{grid}. We solved this nonlinear inversion problem using a standard least squares technique iteratively.

2.3. Nonlinear Inversion Method

[10] In this section, we shall explain the linearization of the nonlinear inversion problem and the estimation of model parameters. The nonlinear inversion problem (equation (11)) is expressed as

$$\mathbf{F}(\mathbf{g}) \approx \mathbf{d}, \quad (12)$$

where

$$\mathbf{g} = \left(g_1^{\mathrm{grid}}, \cdots, g_l^{\mathrm{grid}}, \cdots, g_{N_{\mathrm{grid}}}^{\mathrm{grid}}\right)^{\mathrm{T}} \quad (13)$$

$$\mathbf{d} = \left(d_{111}^{\mathrm{grid}}, \cdots, d_{mni}^{\mathrm{grid}}, \cdots, d_{N_{\mathrm{hyp}}N_{\mathrm{stn}}N_{\mathrm{win}}}^{\mathrm{grid}}\right)^{\mathrm{T}}. \quad (14)$$

We call $\mathbf{g}$ and $\mathbf{d}$ model parameter vector and data vector, respectively. Typically, the nonlinear inversion problem of equation (12) can be inverted by a linearized iterative approach given by [e.g., *Menke*, 1984]

$$\nabla\mathbf{F}\big|_{\mathbf{g}^{(n)}}\delta\mathbf{g}^{(n)} \approx \delta\mathbf{d}^{(n)} \quad (15)$$

$$\mathbf{g}^{(n+1)} = \mathbf{g}^{(n)} + \delta\mathbf{g}^{(n)}, \quad (16)$$

where $\mathbf{g}^{(n)}$ is the estimated model parameter vector, $\delta\mathbf{g}^{(n)} \approx \mathbf{g} - \mathbf{g}^{(\mathrm{n})}$ is the model correction vector, and $\delta\mathbf{d}^{(n)} = \mathbf{d} - \mathbf{F}(\mathbf{g}^{(n)})$ is the residual vector after the nth iteration. $\nabla\mathbf{F}\big|_{\mathbf{g}^{(n)}}$ is the partial derivative matrix for $\mathbf{g}^{(n)}$. If we have a reasonable initial model $\mathbf{g}^{(0)}$, equation (15) can be solved for $\delta\mathbf{g}^{(0)}$ using standard least squares techniques, and a new guess $\mathbf{g}^{(1)}$ can be computed from equation (16). This process can be iterated until the Euclidian length of the vector $\delta\mathbf{g}^{(n)}$ becomes sufficiently small.

[11] We introduced a weight matrix $\mathbf{C}$ to the estimation of $\delta\mathbf{g}^{(n)}$, and minimized the total error E given by

$$E = \left\|\mathbf{C}\delta\mathbf{d}^{(n)} - \mathbf{C}\nabla\mathbf{F}\big|_{\mathbf{g}^{(n)}}\delta\mathbf{g}^{(n)}\right\|^2. \quad (17)$$

The weight matrix $\mathbf{C}$ is ordinarily selected, on the basis of the covariance matrix of the observed data or a priori observation accuracy. In this study, we set

$$\mathbf{C} = \begin{pmatrix} w_{111} & & & & \mathbf{0} \\ & \ddots & & & \\ & & w_{mni} & & \\ & & & \ddots & \\ \mathbf{0} & & & & w_{N_{hyp}N_{stn}N_{win}} \end{pmatrix}, \quad (18)$$

where if $t_{mn}^{\min} \le t_i \le t_{mn}^{\max}$, then $w_{mni} = 1/F(\mathbf{g}^{(n)})_{mni}$, and if $t_i < t_{mn}^{\min}$, $t_{mn}^{\max} < t_i$, then $w_{mni} = 0$. While w_{mni} is the weighting factor for the individual data set, $t_{mn}^{\min}$ and $t_{mn}^{\max}$ are the start and end times of the permitted lapse time range for this analysis, respectively. We selected $w_{mni} = 1/F(\mathbf{g}^{(n)})_{mni}$ in order to prevent strong dependency of the estimated model parameter on the relatively early coda with large energy density. The start time $t_{mn}^{\min}$ was selected so that the earliest portion of the S coda could be avoided. If our approximation of isotropic scattering is not applicable to the real structure, it is difficult to consistently model both early coda, composed mainly by forward scattered waves, and later coda, composed by back scattered waves. Even in such a case, we can stably estimate back scattering coefficient by omitting the earliest portion of the *S* coda from our data set, and then we adopted 1.5 times the travel time of the direct *S* wave as the start time $t_{mn}^{\min}$. The end time $t_{mn}^{\max}$ was set to reduce the effect of multiple scattering. *Hoshiba* [1991] showed that the effect of multiple scattering was reasonably small before the 0.65 time's mean free time. Following his results, we adopted 30 s as the end time $t_{mn}^{\max}$.

[12] As we have a large amount of available data, the present inversion can be an overdetermined least squares problem to estimate $\delta\mathbf{g}^{(n)}$. Even in such a case, the least squares equation may be ill-conditioned because of the nonuniform coverage of the scattering shells related to the data, and some model parameters cannot be stably estimated. Therefore we prefer to introduce the constraints as a priori information of the model parameters to minimize the following value:

$$\phi = \left\|\mathbf{C}\delta\mathbf{d}^{(n)} - \mathbf{C}\nabla\mathbf{F}\big|_{\mathbf{g}^{(n)}}\delta\mathbf{g}^{(n)}\right\|^2 + \theta_c^2\left\|\mathbf{I}\delta\mathbf{g}^{(n)}\right\|^2 + \theta_m^2\left\|\mathbf{D}\delta\mathbf{g}^{(n)}\right\|^2, \quad (19)$$

where matrices $\mathbf{I}$ and $\mathbf{D}$ are the unit matrix and the matrix of spatial Laplacian operator, which produces a vector $\mathbf{D}\delta\mathbf{g}^{(n)}$ of the second differences between scattering coefficient perturbations in adjacent grids, respectively; θ_c^2 and θ_m^2 are nonnegative influence parameters for the constraint. The second term is a constraint to minimize the Euclidian length of the correction vector in each iteration. The third term is a constraint to smooth the spatial variation of the model parameters. According to the standard least squares problem, the condition to minimize ϕ is described as

$$\begin{pmatrix} \nabla\mathbf{F}\big|_{\mathbf{g}^{(n)}}{}^{\mathrm{T}}\mathbf{W_e}\nabla\mathbf{F}\big|_{\mathbf{g}^{(n)}} \\ \theta_m^2\mathbf{W_m} \\ \theta_c^2\mathbf{I} \end{pmatrix}\delta\mathbf{g}^{(n)} \approx \begin{pmatrix} \nabla\mathbf{F}\big|_{\mathbf{g}^{(n)}}{}^{\mathrm{T}}\mathbf{W_e}\delta\mathbf{d}^{(n)} \\ \mathbf{0} \\ \mathbf{0} \end{pmatrix}, \quad (20)$$

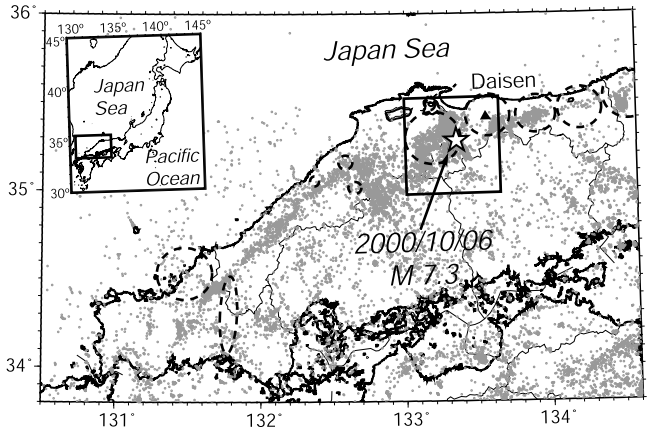

Figure 2. Regional map of southwestern Japan. Rectangle denotes the study area for which the results of the scattering inversion are shown in Figures 8, 9, 11, and 12. Hypocenters of recent shallow earthquakes are shown by gray circles. Dashed lines denote locations of Quaternary volcanoes [*Committee for Catalog of Quaternary Volcanoes in Japan*, 1999]. The hypocenters of the 2000 western Tottori earthquake and Daisen volcano are shown by a star and a triangle, respectively.

where

$$\mathbf{W_e} = \mathbf{C}^T\mathbf{C} \tag{21}$$

$$\mathbf{W_m} = \mathbf{D}^T\mathbf{D}. \tag{22}$$

Equation (20) can be solved more stably than equation (15) in each iteration in order to estimate the model correction vector $\delta\mathbf{g}^{(n)}$.

3. Application to Real Data

3.1. The 2000 Western Tottori Earthquake

[13] At first, we tested presently developed the inversion method by inverting synthetic data, and we then applied it to the real data acquired in and around the focal area of the western Tottori earthquake. The 2000 western Tottori earthquake with M 7.3 occurred on 6 October 2000 in Tottori prefecture, southwestern Japan (Figure 2). In this region, many shallow earthquakes occur constantly along the sea shore of the Japan Sea with a band-shaped distribution in the ENE-WSW direction. The 2000 western Tottori earthquake occurred in this seismic band (Figure 2). In and around the focal area, an active fault named Kamakura-Yama Nanpo fault with a low-activity level had been identified [*Active Fault Research Group*, 1991]. However, the strike of this active fault is not consistent with the fault plane of the 2000 western Tottori earthquake. The active fault seems not to be related to the main shock. It is very important to know how such a large earthquake occurred in this area where a causative active fault has not been detected. Assuming that there are inhomogeneous structures related to the main shock fault in the crust, we try to image the inhomogeneous structures in and around the focal area.

3.2. Data and Analysis

[14] The Joint Group for Dense Aftershock Observation of the 2000 Tottori-ken Seibu Earthquake deployed 60 temporary seismic stations in and around the focal area of the earthquake, and the observation was carried out for about 2 months. Twelve permanent stations are also located in and around the area, which have been operated by Kyoto University, the Japan Meteorological Agency and the National Research Institute for Earth Science and Disaster Prevention [*Joint Group for Dense Aftershock Observation of the 2000 Tottori-ken Seibu Earthquake*, 2001]. We used waveform data acquired at these temporary and permanent stations, and arrival time data picked by the Joint Group for Aftershock Observation.

[15] At first, we determined aftershock hypocenter locations with the software HYPOMH [*Hirata and Matsu'ura*, 1987], and estimated the focal mechanisms of events with M 2.0 to 3.0 from polarity data using the method of *Abers and Gephart* [2001]. In both hypocenter and focal mechanism estimations, we used a one dimensional velocity structure similar to that used routinely by Tottori Observatory, Kyoto University. The velocity structure is shown in Figure 3. We selected 82 events with M 2.0 to 3.0 of hypocenter locations and focal mechanisms estimated with good accuracy, as shown in Figure 4. In this event selection, we also took into consideration the spatial distribution of the hypocenters, because we prefer a good coverage of scattering shells made from a spatially uniform distribution of stations and hypocenters to resolve the spatial variation of scattering coefficient. Figure 5 shows the estimated focal mechanisms of the events. Most of the events have focal mechanisms of left-lateral strike-slip type, similar to the main shock with M 7.3. We selected and used 3567 three-component seismograms observed at 59 stations in Figure 5, taking the quality of the waveform data into consideration.

[16] We set 2459 grids with a 5-km spacing in and around the focal area and with a 10-km spacing in the surroundings, as shown in Figure 6. Circles denote locations of the grids, and gray scale indicates the hit counts defined as the number of envelopes in the estimation of the scattering coefficient in each grid. The hit counts were greater than 2000 in most of the grids in and around the focal area, although much less in peripherals of model space.

3.3. Checkerboard Resolution Test

[17] We checked how well the present inversion method could resolve the spatial distribution of scattering coeffi-

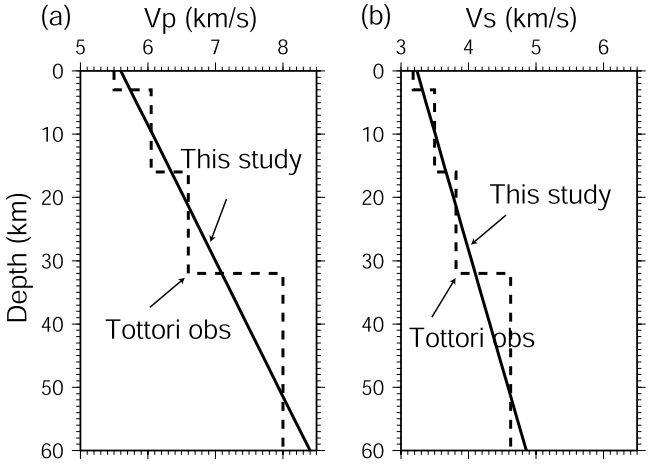

Figure 3. Velocity structures of (a) *P* and (b) *S* waves. Solid lines show one-dimensional depth-dependent velocity structures for hypocenter determination, estimation of focal mechanism, and inversion analysis. Dashed lines denote the velocity structure routinely used for the hypocenter determination in Tottori Observatory of the Disaster Prevention Research Institute, Kyoto University.

cient by the following checkerboard resolution test (CRT). The CRT is often used to evaluate the spatial resolution of inversion problems for seismic wave velocity structures [e.g., *Zhao et al.*, 1992]. In those studies, synthetic travel time data are generated for a medium having a checkerboard pattern of velocity structure, and the employed inversion procedure is used to check how the initial assumed velocity structure is recovered. In the present study, synthetic envelope data were generated for a medium having a checkerboard pattern of scattering coefficient structure. We assumed the presences of 10-km size anomaly zones with large scattering coefficient (g_0 = 0.02 km^{-1}) in the background inhomogeneous media (g_0 = 0.001 km^{-1}). The total of 3567 noise-free synthetic envelope seismograms with a length of 30 s from the origin time, which was the same length as the available waveform data in the following analysis, was generated according to equation (1). In this generating the envelope data, the length of time windows t^{win} for the evaluation of average energy density was 1 s, and we selected the intrinsic absorption parameter $Q_{\mathrm{int}}\,(\omega)^{-1}$ to be 0.0017 in the case of ω = 6 Hz, in reference to the results of multiple lapse time window analysis in this region by *Hoshiba* [1993]. Then we estimated the scattering coefficient in each grid from these synthetic data. We used an initial model with the scattering coefficient of all the grids to be 0.005 km^{-1}, and assumed the same intrinsic absorption parameter as in the generation of the synthetic data. The influence parameters θ_m^2 = 0.01 and θ_c^2 = 0.01 were selected by trial and error, and time windows for coda normalization were 20–28 s from the origin time.

[18] We defined the misfit at the *n*th iteration as

$$\mathrm{misfit}^{(n)} = \left\| \mathbf{Cd} - \mathbf{CF}\left(\mathbf{g}^{(n)}\right) \right\|^2, \tag{23}$$

which is the weighted sum of the squared residual. Figure 7a shows that the misfit is sufficiently reduced after the fifth iteration, and we selected the model after the fifth iteration to be the final result. The results at 8 depth levels in and

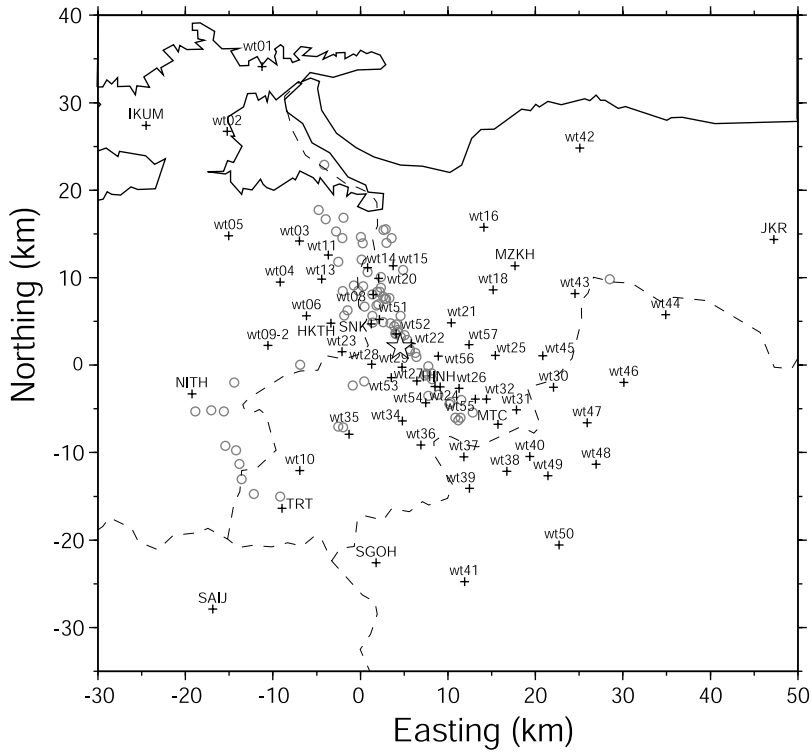

Figure 4. Hypocenters used in the inversion and stations used in the hypocenter determination are shown by open circles and crosses, respectively. The main shock hypocenter is shown by a star.

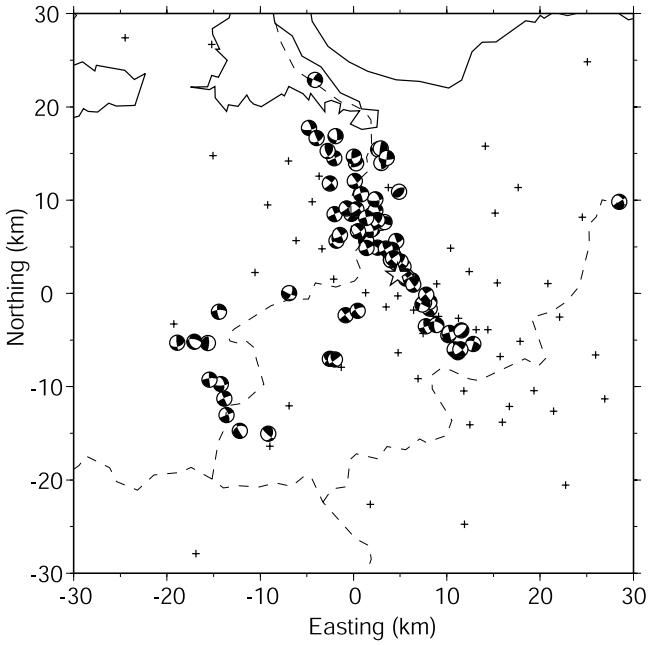

Figure 5. Estimated focal mechanisms plotted by lower hemisphere projection and stations used in the inversion by crosses. The main shock hypocenter is shown by a star.

around the focal area are shown in Figure 8. The checkerboard pattern and the absolute value of scattering coefficient were well recovered near sources and stations at depths of 0, 5, 10, 15, and 20 km, but not recovered well at depths of 25 km and deeper. These features indicate that the spatial variation is resolved very well near the sources and stations, but not well in deep regions and far from the sources and stations, in spite of significant numbers of the hit counts in Figure 6. In the regions of low resolution, the scattering shells which depend on geometries of the sources and stations have similar shapes to each other. In such a case, the coda energy density corresponding to the scattered wave from the regions is not sensitive to the geometries and spatial variation of the scattering coefficient.

3.4. Spatial Variation in and Around the Focal Area of the 2000 Western Tottori Earthquake

[19] We first produced normalized envelope seismograms from three-component seismograms after processing the signals with a band-pass filter (4.5–9.0 Hz), according to the right-hand side of equation (10). All the parameters for the analysis had the same values as those in the CRT. The scattering coefficient of all the grids in the initial model was selected to be 0.005 km^{-1} in reference to *Hoshiba* [1993]. As in the case of the CRT, The misfit of defined by equation (23) was also sufficiently decreased after five iterations (Figure 7b), reducing from 3.79×10^4 to 1.91×10^4. The estimated distributions of scattering coefficient at eight depth levels in and around the focal area are shown in

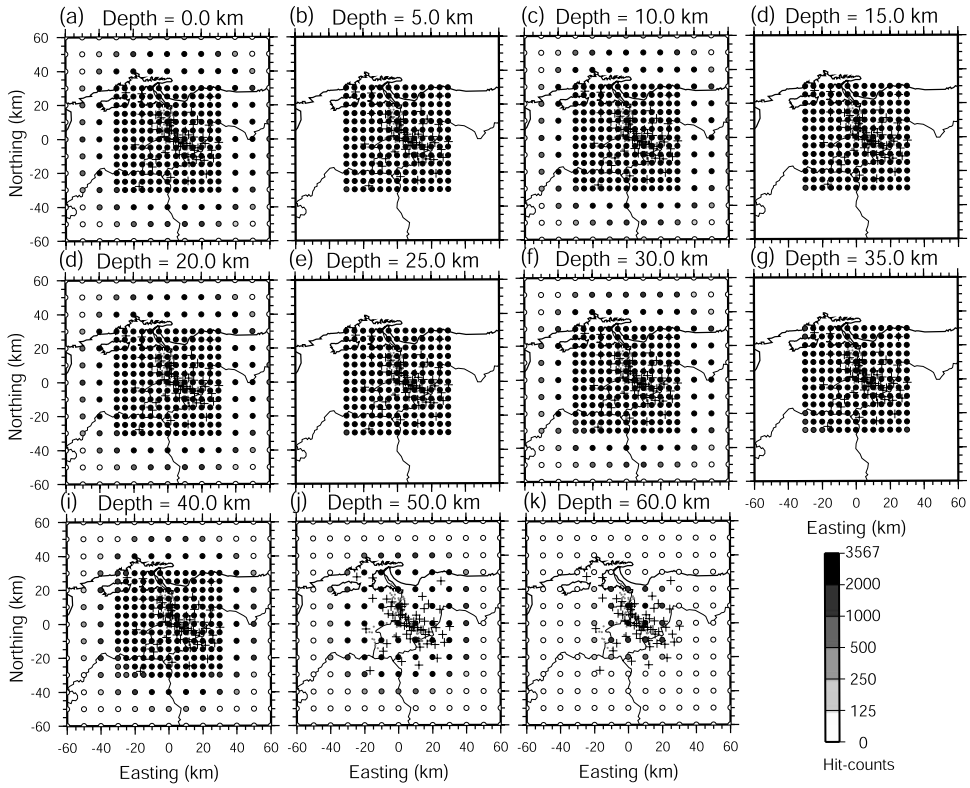

Figure 6. Grids for estimated scattering coefficients shown by circles at depth levels of (a) 0 km, (b) 5 km, (c) 10 km, (d) 15 km, (e) 20 km, (f) 25 km, (g) 30 km, (h) 35 km, (i) 40 km, (j) 50 km, and (k) 60 km. Gray scale denotes hit counts in each grid.

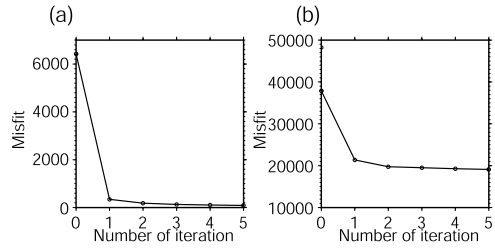

Figure 7. Misfits in each iteration of the inversion defined by equation (23) for (a) checkerboard resolution test and (b) inversion applying to real data.

Figure 9. Some of the large scattering coefficient zones (LSZs) are distributed along and around the main shock fault at depths of 0 to 10 km (Figures 9a–9c). These LSZs extend to a deeper portion of both edges of the main shock fault (Figure 9d). LSZs are also detected in the mid and lower crust. They are localized below the northwestern part of the main shock fault at depths of 15 and 20 km (Figures 9d and 9e). Remarkable LSZs near Mount Daisen, a Quaternary volcano, are distributed at all depth levels, although spatial resolution is poor at depths of 25 km and deeper. Moho discontinuity was also detected as an LSZ at depths of 20, 25 and 30 km (Figures 9f, 9g, and 9h). These LSZs at depths of 20 km and shallower are considered to be sufficiently large to be resolved by the present inversion, considering their size and the results of the CRT. Inhomogeneous structures related to the LSZs are discussed in section 4. Remarkable energy arrivals from the LSZs below the northern part of the main shock fault and Moho discontinuity can be seen in the observed and the model-predicted envelopes shown in Figure 10. Model-predicted envelopes agree well with the general features of observed envelopes, although the model-predicted envelopes seem to be smoother than the observed envelopes and show vague energy arrivals from the LSZs. Remarkable energy arrivals corresponding to the LSZs along the main shock fault could not be recognized in both model-predicted and observed envelopes in Figure 10. The reason for this can be interpreted that the energy from these LSZs arrives in the relatively early portion of coda following the direct *S* waves. Although the very early portion of coda was not used in our inversion, the existence of these LSZs along the main shock fault is needed to explain the observed different decay gradients among many coda envelopes in the relatively early portion.

[20] The obtained LSZs were also checked for resolution and robustness against noise contamination using the restoring resolution test (RRT) [e.g., *Zhao et al.*, 1992], which is effective to check how well the LSZs with various

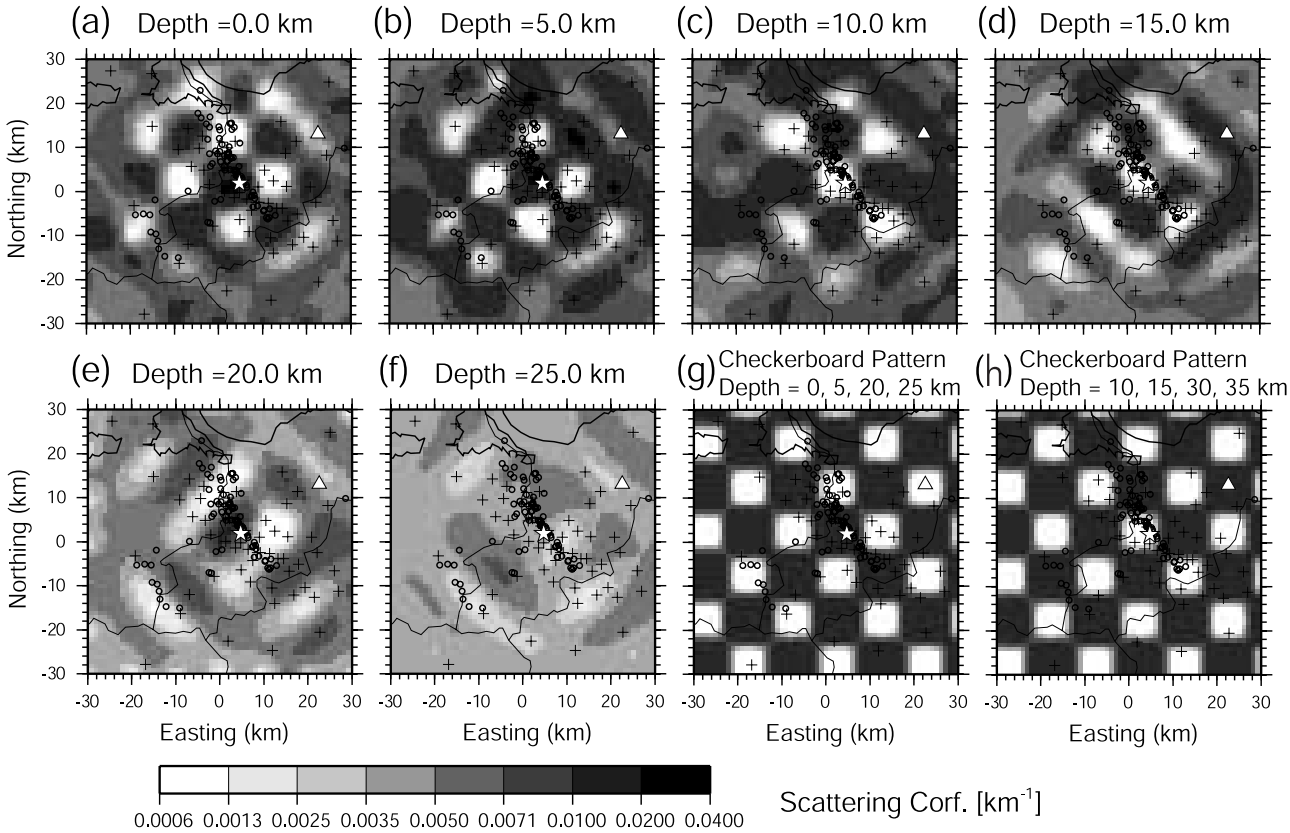

Figure 8. Results of checkerboard resolution test at depth levels of (a) 0 km, (b) 5 km, (c) 10 km, (d) 15 km, (e) 20 km, and (f) 25 km. Gray scale denotes values of estimated scattering coefficient. Hypocenters and stations are shown by circles and crosses, respectively. The main shock hypocenter and Daisen volcano are shown by a star and a triangle, respectively. Assumed checkerboard pattern at depths of (g) 0, 5, 20, and 25 km and (h) 10, 15, 30, and 35 km.

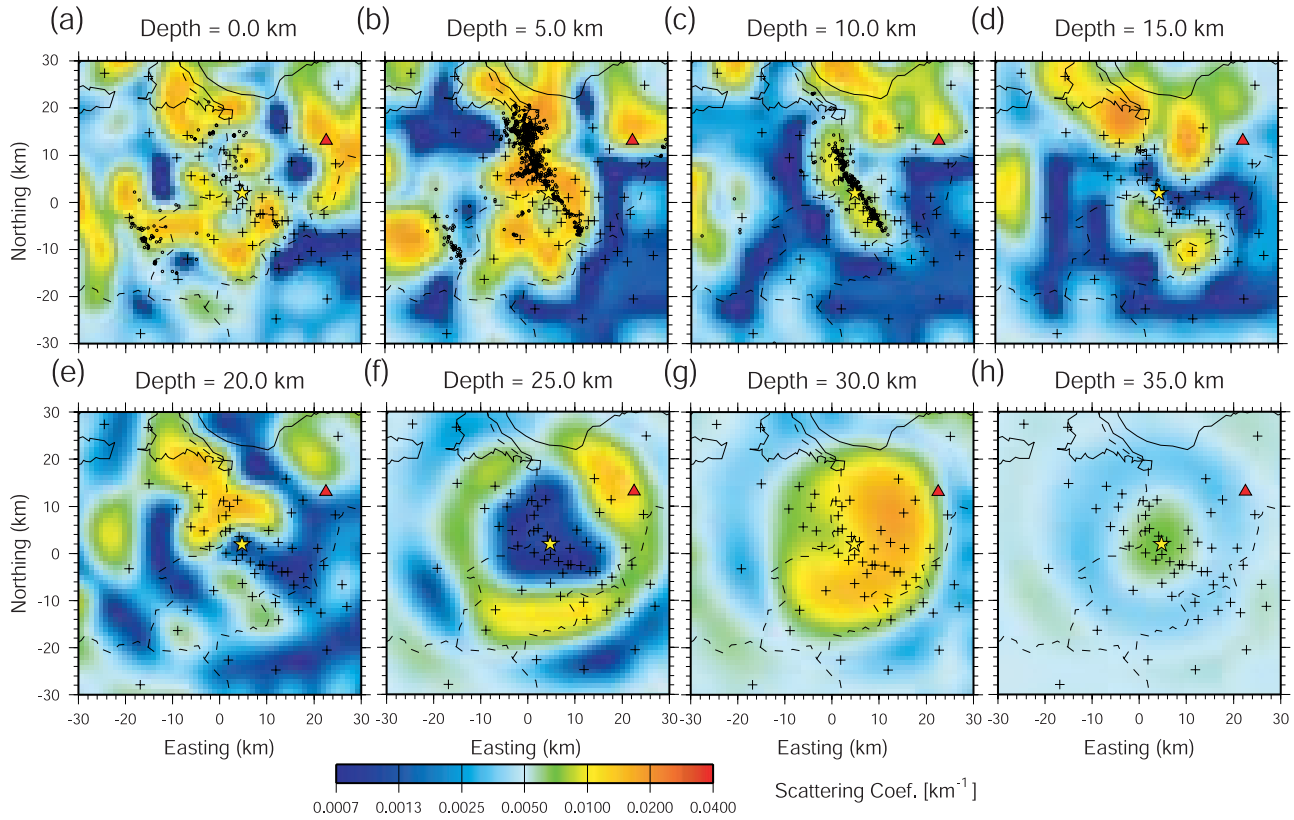

Figure 9. Distribution of scattering coefficient in and around the focal area of the 2000 western Tottori earthquake at depth levels of (a) 0 km, (b) 5 km, (c) 10 km, (d) 15 km, (e) 20 km, (f) 25 km, (g) 30 km, and (h) 35 km. Color scale denotes values of scattering coefficient. The epicenter of the main shock and Daisen volcano are shown by a star and a triangle, respectively. Small circles denote aftershocks occurring within 2.5 km from each depth revel during the period 15 to 25 October 2000 [*Joint Group of Dense Aftershock Observation of the 2000 Tottori-ken Seibu Earthquake*, 2001].

sizes could be resolved. Synthetic data for the test were generated from the obtained results (Figure 9) by adding Gaussian noise of 20% to the synthetic energy density, which is nearly equal to the level of energy perturbation in the envelopes observed at each station. Since the level is much larger than that of ground and electric noise, such an energy perturbation is caused by the complexity of wave propagation, which cannot be expressed in our simplified model. The synthetic data with the noise were inverted using the same parameters as in the inversion of the real

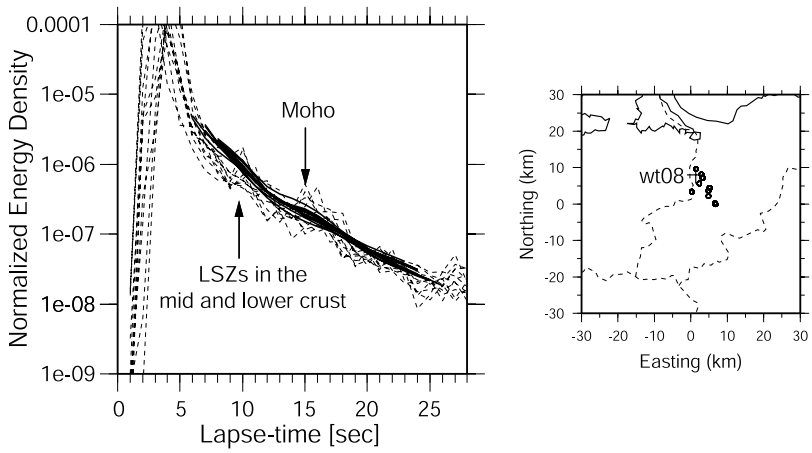

Figure 10. Examples of observed and model-predicted envelopes. Solid lines and dashed lines denote model-predicted and observed envelopes at station wt08. The station wt08 and hypocenters are indicated in the inset map by a cross and circles.

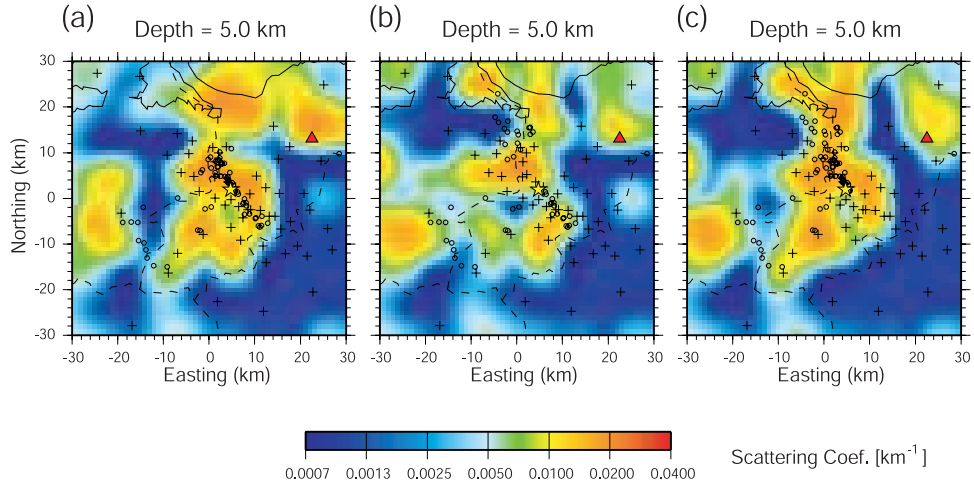

Figure 11. Test with data reselection for scattering coefficient at the depth of 5 km by removing events (a) in the northern part, (b) in the central part, and (c) in the southern part of the aftershock area. All the symbols are the same as Figure 8.

data. Obtained patterns of the RRT well recovered and are very similar to the original ones. These results indicate that the obtained distribution of LSZs and its resolution are robust to random noise contamination for the data.

[21] The results of the CRT and RRT show the feasibility of the inversion method and good spatial resolution in and around the focal area of interest. Further, we made an additional test to check reliability for the existence of the LSZs along the main shock fault. At first, we classified the 82 events into four groups according to their hypocenter locations, northern, central, southern, and surrounding groups. Next, we made three data sets which were removed one group from the original data set. Then we inverted these data sets to estimate the distribution of the scattering coefficient. The obtained distribution images of scattering coefficient at a depth of 5 km for the three data sets are shown in Figure 11. They are similar to that obtained from the original data set (Figure 9b). We obtained almost identical results also at other depth levels. These indicate that three different distributions of hypocenters used do not strongly affect estimated distribution of scattering coefficient, which shows that the LSZs along the main shock fault are not artifact.

4. Discussion

4.1. Inhomogeneous Structure Along the Main Shock Fault in the Upper Crust

[22] Reflected and scattered waves from nearly vertical faults have been detected along the San Andreas fault system [e.g., *Hole et al.*, 1996; *Parsons*, 1998; *Nishigami*, 2000]. *Hole et al.* [1996] and *Parsons* [1998] detected reflected waves from the faults by seismic reflection surveys. *Parsons* [1998] concluded that the Hayward fault extends down to the Moho discontinuity and cuts the entire crust considering the shape of reflection surface. *Nishigami* [2000] estimated the spatial distribution of relative scattering strength from coda envelopes of local earthquakes, and detected strongly inhomogeneous structures along the faults. In the present study, we also detected distinct LSZs distributed exactly along the main shock fault at a depth of 10 km. This suggests that the LSZs are related to the main shock fault of the 2000 western Tottori earthquake. These fault structures have also been investigated using fault trapped waves. *Nishigami et al.* [2002] investigated fault trapped waves at stations along the main shock fault. The results show the existence of fault-damaged zones below the stations, and the estimated width of the fault-damaged zone along the main shock fault is about 20 m. Even in the most developed fault-damaged zone, such as that of the Landers earthquake in 1994, the estimated width of the damaged zone was about 200 m [*Li et al.*, 1994]. In the present study we used seismograms with a band-pass filter (4.5–9.0 Hz) whose wavelength is about several hundred meters, assuming the *S* wave velocity to be 3–4 km/s. Although this is larger than the typical width of fault-damaged zones, strands of the fault-damaged zones can effectively scatter seismic waves with larger wavelength and can be imaged as the LSZs along the main shock fault.

[23] The distinct LSZs at a depth of 5 km are distributed widely along the main shock fault. Figure 12 shows the distribution of lineaments detected from aerial photograph interpretations of active structures by *Inoue et al.* [2002]. They also found faults, fault gouges, horizontal striations on the faults, and intrusions near the faults along the lineaments. The distribution of lineaments has a good spatial correlation with the distribution of the LSZs at a depth of 5 km (Figure 12). These results suggest that the 2000 western Tottori earthquake occurred in a strongly inhomogeneous zone, although no causative active faults had been detected [*Active Fault Research Group*, 1991]. We may be able to detect subsurface inhomogeneous structures that cause large earthquakes by using the present inversion method.

[24] Next we discuss the spatial distribution of scattering coefficient along the fault plane. The depth distribution is shown in Figure 13, together with aftershock hypocenters [*Joint Group for Dense Aftershock Observation of the 2000 Tottori-ken Seibu Earthquake*, 2001] and coseismic slip of the main shock [*Iwata and Sekiguchi*, 2002]. We can see a good spatial correlation between the LSZs and the aftershock activity. An asperity with large coseismic slip is located in a

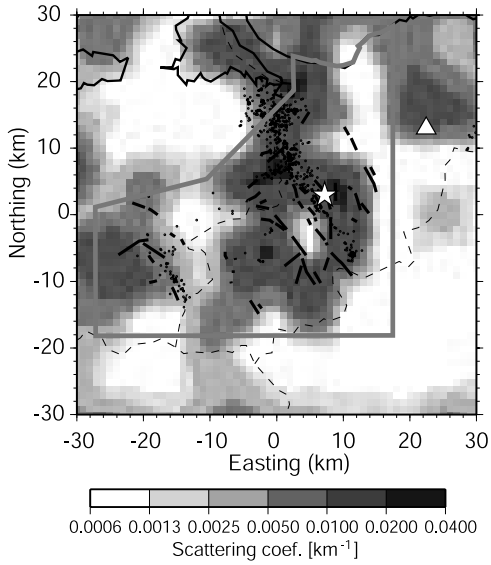

Figure 12. Lineaments in an area of aerial photographic interpretation performed by *Inoue et al.* [2002] as a polygon drawn by a gray solid line. Lineaments are shown by solid lines. Estimated distribution of scattering coefficient at a depth of 5 km is shown in gray scale. Circles denote aftershocks occurring at a depth range of 2.5–7.5 km during the same period as Figure 9 [*Joint Group of Dense Aftershock Observation of the 2000 Tottori-ken Seibu Earthquake*, 2001].

zone with relatively low scattering coefficient between the two prominent LSZs (Figure 13). *Revenaugh* [1995] imaged scattering structures of the focal area of the Landers earthquake in 1994 using teleseismic events. They detected the good correlation among scattering intensity, aftershock activity, and coseismic slip. *Nishigami* [2000] also showed that focal areas of large earthquakes along the San Andreas fault system in California were bounded by strongly inhomogeneous zones with large scattering strength, which he interpreted as heavily damaged zones. The detected relationship among scattering coefficient, aftershock activity and asperity along the main shock fault of the 2000 western Tottori earthquake (Figure 13) is consistent with these previous results. Relatively homogeneous zones among heavily inhomogeneous zones can store stress and cause a relatively large amount of slip at the time of large earthquakes. On the contrary, coseismic slip in LSZs is presently small. This suggests that heavily damaged areas with large scattering strength can not store stress because such damaged regions seem to release stress by small earthquakes, aseismic slip, and volumetric creep deformation.

4.2. Inhomogeneous Structure in the Mid and Lower Crust

[25] Clear LSZs at the depth of 15 to 20 km are distributed below the northern part of the main shock fault (Figures 9 and 13). LSZs in the mid and lower crust were also detected beneath the northeastern Japan arc. *Ogawa et al.* [2001] carried out MT observations to estimate resistibility structure in the Ou backbone range of the northeastern Japan arc. They found that the low-resistibility zones were distributed in the downward extension of the Senya fault near the volcanic front, and that there was a good spatial correlation among the low-resistibility zones, seismic scatterers [*Asano et al.*, 1999], and seismic low-velocity zones [*Nakajima et al.*, 2001]. In that study, it was interpreted that the low-resistibility zones showed the existence of fluids in the mid and lower crust. Localized fluid-filled cracks distributed in the area can scatter seismic waves effectively as LSZs. *Nakajima and Hasegawa* [2003] showed a clear seismic low-velocity anomaly, which exhibited low V_p, low V_s, and high V_p/V_s values, extending from the uppermost mantle to active volcanoes and to the focal area of the 1962 Northern Miyagi earthquake of M 6.5, in northeastern Japan. The low-velocity zone below the main shock fault of the 1962 Northern Miyagi earthquake also has a good correlation with the low-resistibility zone [*Mitsuhata et al.*, 2001]. They concluded that the low-velocity zone indicates the existence of partial melt and/or H_2O supplied to the upper crust from the partial melting zone in the lower crust. The

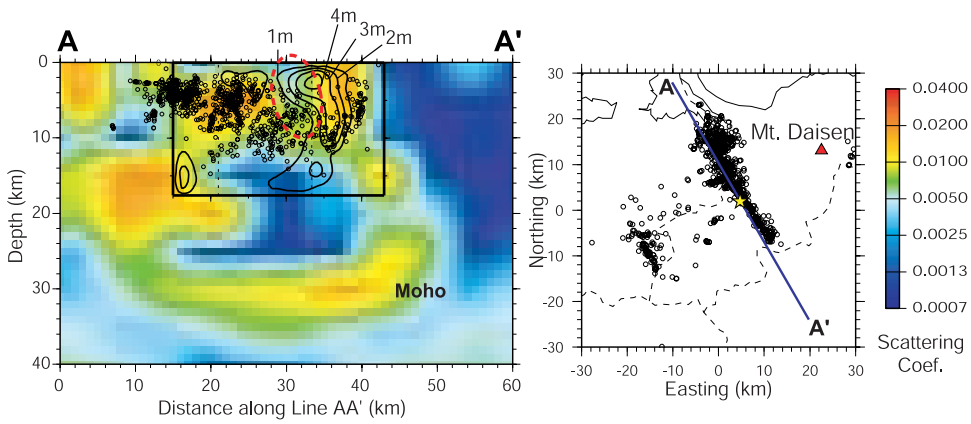

Figure 13. Depth distribution of scattering coefficient along the main shock fault plane. A star and contours denote the rupture initiation point and coseismic slip of the main shock [*Iwata and Sekiguchi*, 2002], respectively, with circles for the same aftershocks as Figures 9 and 12. A red ellipse denotes the exceptional area with relatively small scattering coefficient in the main shock fault. Inset map indicates the line along which the distribution of scattering coefficient is shown.

focal area of the 2000 western Tottori earthquake was also located near Quaternary volcanoes [*Committee for Catalog of Quaternary Volcanoes in Japan*, 1999] (Figure 2) and near a low-velocity zone in the crust, which also exhibited low V_p, low V_s, and high V_p/V_s [*Shibutani and Maeda*, 2002]. The LSZs below the northern part of the focal area in the mid and lower crust were located in the low-velocity zone, although spatial resolution of their results was not enough to be compared with our results. The low-velocity zone shows a band-shaped distribution, parallel to the Quaternary volcanic front. The low-velocity band at the depth of 30 km was located about 30 km south of the surface distribution of the Quaternary volcanoes, and the low-velocity band in the upper crust was located near the coast of the Japan Sea. This type of distributions is similar to that found in northeastern Japan by *Nakajima and Hasegawa* [2003]. The interpretation of the existence of fluid there is consistent with the occurrence of low-frequency microearthquakes [*Ohmi et al.*, 2002] near the Moho discontinuity in this area.

5. Conclusions

[26] We developed a new inversion method to estimate 3-D spatial distribution of scattering coefficient, using envelope seismograms of *S* coda. The method can take into consideration realistic models in velocity structure, source radiation, and scattering attenuation, which enables to image the distribution of scattering coefficient with high resolution.

[27] The presently developed inversion method was applied to the real data acquired in and around the focal area of the 2000 western Tottori earthquake with *M* 7.3. The inverted image shows that most prominent LSZs are distributed along and around the main shock fault. These LSZs suggest the existence of fault-damaged zones. An exceptionally small scattering coefficient zone in the LSZs along the main shock fault perhaps corresponds to the asperity with large coseismic slip. LSZs were also detected in the mid to lower crust below the northern part of the main shock fault. Other LSZ was detected near Daisen volcano, which suggests that the LSZs are related to the deep structure of Quaternary volcanoes.

[28] The present inversion showed that the 2000 western Tottori earthquake occurred in a strongly inhomogeneous area with large scattering coefficients, where causative active faults have not been detected in the focal area. The present inversion method may be effective for detecting such buried structure that causes large earthquakes.

[29] **Acknowledgments.** We appreciate the Joint Group for Dense Aftershock Observation of the 2000 Tottori-ken Seibu earthquake for allowing us to use their waveform data and arrival time data. Seismograph stations used in this study include permanent stations operated by the Japan Meteorological Agency (JMA), the National Research Institute for Earth Science and Disaster Prevention (NIED), Earthquake Research Institute, University of Tokyo (ERI), and the Disaster Prevention Research Institute, Kyoto University (DPRI). J. Revenaugh and K. Nishigami provided thoughtful reviews, which improved the manuscript. All the figures were drawn with the software GMT [*Wessel and Smith*, 1991].

References

Abers, G. A., and J. W. Gephart (2001), Direct inversion of earthquake first motions for both the stress tensor and focal mechanisms and application to southern California, *J. Geophys. Res.*, *106*, 26,523–26,540.

Abubakirov, I. R., and A. A. Gusev (1990), Estimation of scattering properties of lithosphere of Kamchatka based on Monte-Carlo simulation of record envelope of a near earthquake, *Phys. Earth Planet. Inter.*, *64*, 52–67.

Active Fault Research Group (1991), *Active Faults in Japan*, new ed., 437 pp., Univ. of Tokyo Press.

Aki, K. (1969), Analysis of the seismic coda of local earthquakes as scattered waves, *J. Geophys. Res.*, *74*, 613–631.

Aki, K. (1980), Attenuation of shear-waves in the lithosphere for frequencies from 0.05 to 25 Hz, *Phys. Earth Planet. Inter.*, *21*, 50–60.

Aki, K., and B. Chouet (1975), Origin of coda waves: Source, attenuation and scattering effect, *J. Geophys. Res.*, *80*, 3322–3342.

Asano, Y., et al. (1999), Spatial distribution of seismic scatterers beneath the Ou backbone range, northeastern Japan (in Japanese with English abstract), *J. Seismol. Soc. Jpn.*, *52*, 379–394.

Chen, X., and L. T. Long (2000), Spatial distribution of relative scattering coefficients determined from microearthquake coda, *Bull. Seismol. Soc. Am.*, *90*, 512–524.

Committee for Catalog of Quaternary Volcanoes in Japan (1999), Catalog of Quaternary volcanoes in Japan, *Bull. Volcanol. Soc. Jpn.*, *44*, 285–289.

Fehler, M., M. Hoshiba, H. Sato, and K. Obara (1992), Separation of scattering and attenuation for the Kanto-Tokai region, Japan, using measurements of *S*-wave energy versus hypocentral distance, *Geophys. J. Int.*, *108*, 787–800.

Hirata, N., and M. Matsu'ura (1987), Maximum-likelihood estimation of hypocenter with origin time eliminated using nonlinear inversion technique, *Phys. Earth Planet. Inter.*, *47*, 50–61.

Hole, J. A., H. Thybo, and S. L. Klemperer (1996), Seismic reflections from the near-vertical San Andreas Fault, *Geophys. Res. Lett.*, *23*, 237–240.

Hoshiba, M. (1991), Simulation of multiple-scattered coda wave excitation based on the energy conservation law, *Phys. Earth Planet. Inter.*, *67*, 123–136.

Hoshiba, M. (1993), Separation of scattering attenuation and intrinsic absorption in Japan using the multiple lapse time window analysis of full seismogram envelope, *J. Geophys. Res.*, *98*, 15,809–15,824.

Inoue, D., K. Miyakoshi, K. Ueta, A. Miyawaki, and K. Matuura (2002), Active fault study in the 2000 Tottori-ken Seibu earthquake area (in Japanese with English abstract), *J. Seismol. Soc. Jpn.*, *54*, 557–573.

Iwata, T., and H. Sekiguchi (2002), Source process and near-source ground motion during the 2000 Tottori-ken Seibu earthquake (in Japanese), *Mon. Earth*, special issue, *38*, 182–188.

Joint Group for Dense Aftershock Observation of the 2000 Tottori-ken Seibu Earthquake (2001), Aftershock distribution of the 2000 Tottori-ken Seibu earthquake determined by dense aftershock observation, paper presented at Japan Earth and Planetary Sciences Joint Meeting, Tokyo.

Li, Y. G., K. Aki, D. Adams, A. Hasemi, and W. H. K. Lee (1994), Seismic guided waves trapped in the fault zone of the Landers, California, earthquake of 1992, *J. Geophys. Res.*, *99*, 11,705–11,722.

Mayeda, K., S. Koyanagi, M. Hoshiba, K. Aki, and Y. Zeng (1992), A comparative study of scattering, intrinsic, and coda Q^{-1} for Hawaii, Long Valley, and central California between 1.5 and 15.0 Hz, *J. Geophys. Res.*, *97*, 6643–6659.

Menke, W. (1984), *Geophysical Data Analysis: Discrete Inverse Theory*, 285 pp, Academic, San Diego, Calif.

Mitsuhata, Y., Y. Ogawa, M. Mishina, T. Kono, T. Yokokura, and T. Uchida (2001), Electromagnetic heterogeneity of the seismogenic region of 1962 *M* 6.5 northern Miyagi earthquake, northeastern Japan, *Geophys. Res. Lett.*, *28*, 4371–4374.

Nakajima, J., and A. Hasegawa (2003), Tomographic imaging of seismic velocity structure in and around the Onikobe volcanic area, northeastern Japan: Implications for fluid distribution, *J. Volcanol. Geotherm. Res.*, *127*, 1–18.

Nakajima, J., T. Matsuzawa, A. Hasegawa, and D. Zhao (2001), Three-dimensional structure of V_p, V_s, and V_p/V_s beneath northeastern Japan: Implications for arc magmatism and fluids, *J. Geophys. Res.*, *106*, 21,843–21,857.

Nishigami, K. (1991), A new inversion method of coda waveforms to determine spatial distribution of coda scatterers in the crust and uppermost mantle, *Geophys. Res. Lett.*, *18*, 2225–2228.

Nishigami, K. (1997), Spatial distribution of coda scatterers in the crust around two active volcanoes and one active fault system in central Japan: Inversion analysis of coda envelope, *Phys. Earth Planet. Inter.*, *104*, 75–89.

Nishigami, K. (2000), Deep crustal heterogeneity along and around the San Andreas fault system in central California and its relation to the segmentation, *J. Geophys. Res.*, *105*, 7983–7998.

Nishigami, K., I. Doi, T. Mizuno, K. Tadokoro, and A. Shimokawa (2002), Investigation for deep structures of the mainshock fault of the 2000 western Tottori earthquake (in Japanese), *Mon. Earth*, special issue, *38*, 174–181.

Obara, K. (1997), Simulations of anomalous seismogram envelopes at coda portions, *Phys. Earth Planet. Inter.*, *104*, 109–125.

Ogawa, Y., et al. (2001), Magnetotelluric imaging of fluids in intraplate earthquake zones, NE Japan back arc, *Geophys. Res. Lett.*, *28*, 3741–3744.

Ohmi, S., K. Watanabe, T. Shibutani, N. Hirano, and S. Nakao (2002), The 2000 western Tottori Earthquake—Seismic activity revealed by the regional seismic networks, *Earth Planets Space*, *54*, 819–830.

Parsons, T. (1998), Seismic-reflection evidence that the Hayward fault extends into the lower crust of the San Francisco Bay area, *Bull. Seismol. Soc. Am.*, *88*, 1212–1223.

Revenaugh, J. (1995), Relation of the 1992 Landers, California, earthquake sequence to seismic scattering, *Science*, *270*, 1344–1347.

Sato, H. (1977), Energy propagation including scattering effects single isotropic scattering approximation, *J. Phys. Earth*, *25*, 27–41.

Sato, H., and M. C. Fehler (1998), *Seismic Wave Propagation and Scattering in the Heterogeneous Earth*, 308 pp., Springer-Verlag, New York.

Shibutani, T., and Y. Maeda (2002), Three-dimensional seismic velocity structure in and around the focal area of the 2000 western Tottori earthquake (in Japanese), *Mon. Earth*, special issue, *38*, 203–208.

Wessel, P., and W. H. F. Smith (1991), Free software helps map and display data, *Eos Trans. AGU*, *72*, 441, 445–446.

Zeng, Y., F. Su, and K. Aki (1991), Scattering wave energy propagation in a random isotropic scattering medium 1. Theory, *J. Geophys. Res.*, *96*, 607–619.

Zhao, D., A. Hasegawa, and S. Horiuchi (1992), Tomographic imaging of *P* and *S* wave velocity structure beneath northeastern Japan, *J. Geophys. Res.*, *97*, 19,909–19,928.

Y. Asano, National Research Institute for Earth Science and Disaster Prevention, Tsukuba 305-0006, Japan. (asano@bosai.go.jp)

A. Hasegawa, Research Center for Prediction of Earthquakes and Volcanic Eruptions, Graduate School of Science, Tohoku University, Sendai 980-8578, Japan.